INTERNATIONAL JOURNAL FOR NUMERICAL METHODS IN FLUIDS
Int. J. Numer. Meth. Fluids 2001; **35**: 785–808

On the accuracy of one-dimensional models of steady converging/diverging open channel flows

M. E. Hubbard*,[1]

The University of Cambridge, DAMTP, Cambridge, U.K.

SUMMARY

Shallow water flows through open channels with varying breadth are commonly modelled by a system of one-dimensional equations, despite the two-dimensional nature of the geometry and the solution. In this work steady state flows in converging/diverging channels are studied in order to determine the range of parameters (flow speed and channel breadth) for which the assumption of quasi-one-dimensional flow is valid. This is done by comparing both exact and numerical solutions of the one-dimensional model with numerical solutions of the corresponding two-dimensional flows. It is shown that even for apparently gentle constrictions, for which the assumptions from which the one-dimensional model is derived are valid, significant differences can occur. Furthermore, it is shown how the nature of the flow depends on the manner in which the boundary conditions are applied by contrasting the solutions obtained from two commonly used approaches. A brief description is also given of the numerical methods, developed recently for the solution of the one- and two-dimensional shallow water equations, and used to produce the results presented in this paper. Copyright © 2001 John Wiley & Sons, Ltd.

KEY WORDS: breadth variation; open channel flows; quasi-one-dimensional models; shallow water equations; steady state

1. INTRODUCTION

For speed and simplicity, one-dimensional models are often used in the modelling of two-dimensional shallow water flows. An example of this is the prediction of the steady flow through an open channel with variable breadth. However, the validity of the one-dimensional model is limited by the assumptions made in its derivation and its accuracy is bound to decrease as the variations in the channel geometry become more severe and the transverse acceleration induced in the flow gains in significance. Not only are there quantitative differences between the one- and two-dimensional solutions, but the flows obtained may also exhibit major differences in their qualitative features giving, for example, differing predictions of the existence of hydraulic jumps.

* Correspondence to: School of Computing, The University of Leeds, Leeds LS2 9JT, U.K. Tel.: +44 113 233 5459.
[1] E-mail: meh@comp.leeds.ac.uk

Received March 1999
Revised June 2000

In this work we examine the range of flow parameters (flow speed and magnitude of constriction) for which the one-dimensional model of steady state shallow water flow through a channel of varying breadth accurately represents the full two-dimensional solution. The investigation is used to highlight the limitations of the one-dimensional model as well as to point out those quantities that it is able to predict accurately, especially when the flow exhibits genuine two-dimensional features and the assumptions underlying the one-dimensional model break down.

Close examination of the mathematical and numerical models also reveals the dramatic effect that changing the form of the boundary conditions can have on the solution, so the results obtained from two commonly used boundary procedures have been compared in order to illustrate the care which must be taken, particularly when choosing boundary conditions for the modelling of transcritical flows.

The one- and two-dimensional shallow water models employed are described in Sections 2 and 3 respectively, along with brief descriptions of the new numerical methods that have been developed and used to approximate them. In one dimension, a brief derivation of a family of exact solutions to the equations is also given. This is presented for completeness, but the underlying analysis is straightforward and is applied to closely related problems in many standard texts, e.g. References [1,2]. The comparison between the two different models is carried out in Section 4 using the numerical techniques described in the preceding sections. This is followed by brief conclusions about the validity of the simpler model and the various forms of boundary condition.

2. THE ONE-DIMENSIONAL MODEL

In one dimension, shallow water flow through an open channel of rectangular cross-section and variable breadth can be modelled by the equations

$$\begin{pmatrix} Bd \\ Bdu \end{pmatrix}_t + \begin{pmatrix} Bdu \\ Bdu^2 + \frac{1}{2} gBd^2 \end{pmatrix}_x = \begin{pmatrix} 0 \\ \frac{1}{2} gd^2 B_x \end{pmatrix} \tag{2.1}$$

in which d represents the depth of the flow, u is its velocity, $B = B(x)$ is the variable breadth of the channel and g is the acceleration due to gravity (see, e.g. Reference [3] for their derivation). Essentially, Equation (2.1) can be derived from the more general two-dimensional shallow water model under the assumption that $B_x = O(\epsilon)$ for $\epsilon \ll 1$, so that the transverse acceleration of the flow is negligible in comparison with the longitudinal acceleration. In these circumstances the variables d and u are considered to be breadth-averaged quantities. Only steady state solutions are considered in this work, for which the time derivatives are zero. They are only included in Equation (2.1) because they are often used as a numerical device to converge to steady solutions. This technique is used in the schemes presented here which provide the approximate solutions of Section 4.

Exact steady state solutions of Equation (2.1) are simple to construct (see, e.g. Reference [4], standard texts [1,2] and related work on the modelling of variable bed topography [5–7], for which this analysis is far more commonly carried out). For a converging/diverging channel with continuously varying breadth, the steady solutions of Equation (2.1) can be divided into four categories:

(A) continuous—purely subcritical (possibly critical at the most narrow point of the channel, the throat);
(B) discontinuous—subcritical at inflow, passing smoothly to supercritical at the throat, then back to subcritical via a stationary hydraulic jump in the diverging region of the channel, remaining so until outflow;
(C) continuous—subcritical at inflow, passing smoothly to supercritical at the throat of the channel, and remaining supercritical to outflow;
(D) continuous—purely supercritical (possibly critical at the throat).

The particular form taken by the steady solution depends on the boundary conditions that are applied at the entrance and the exit of the channel section being modelled. Much analysis has been applied to flows in channels of infinite length [6,7] to determine the steady state that is left behind around an obstacle as $t \to \infty$, but in reality the domain of interest is finite and boundary conditions must be applied at an appropriate distance from the obstacle: their effect is studied here.

The simplest cases are A and D. Integration of the steady equations leads straightforwardly to two quantities that remain constant throughout the channel. These are the total discharge

$$Q = Bdu \tag{2.2}$$

and the total head

$$H_T = \frac{u^2}{2g} + d = \frac{Q^2}{2gB^2d^2} + d \tag{2.3}$$

Given that values for Q and H_T can be deduced from the boundary conditions, combining Equations (2.2) with (2.3) results in

$$d^3 - H_T d^2 + \frac{Q^2}{2gB^2H_T^3} = 0 \tag{2.4}$$

an algebraic equation relating the depth of the flow d to the local channel breadth B. This has a pair of physically admissible (positive) solutions for d, one representing subcritical flow and the other supercritical flow, on condition that

$$\frac{B}{B_{in}} \geq F_{in}\left(\frac{3}{F_{in}^2 + 2}\right)^{3/2} \tag{2.5}$$

for all values of B in the given channel geometry, where $F_{\text{in}} = u_{\text{in}}/\sqrt{gd_{\text{in}}}$ is the local Froude number specified at inflow. The solution chosen by Equation (2.1) depends on the boundary conditions applied (unless Q and H_{T} are the two quantities specified, in which case the choice remains open).

When equality holds in Equation (2.5) for some value of B within the channel geometry, the flow becomes critical for the values of Q and H_{T} implied by the boundary conditions. However, any critical point of the flow must lie at the throat of the channel so, unless equality is satisfied there, the inlet values of Q and/or H_{T} change automatically to satisfy the boundary condition at inflow *and* the critical condition at the throat ($F = 1$ when $B = B_{\min}$). The flow is then of type B or C. Furthermore, the variation of the Froude number upstream of the critical point in such situations is uniquely defined, being the subcritical solution ($0 < F < 1$) of the equation

$$F^2\left(\frac{3}{F^2+2}\right)^3 = \left(\frac{B_{\min}}{B}\right)^2 \tag{2.6}$$

This implies that the Froude number at inflow is fixed by the channel geometry, taking the same value whenever the solution is transcritical (so F is not a practical choice for specification as an inflow boundary condition). The new values of Q and H_{T} for the smooth region of the flow that surrounds the critical point can be calculated by combining the subcritical inflow boundary condition with this inflow Froude number.

Downstream of the critical point, the flow type (B or C) is determined by the outflow boundary conditions. Initially, since the flow is continuous through the critical point, the solution retains the upstream values of Q and H_{T} but switches to the supercritical branch of Equation (2.4) downstream of the throat. If no jump occurs the supercritical solution values found using Equation (2.4) are retained throughout the rest of the channel.

When a stationary hydraulic jump occurs (which must always be from supercritical flow to subcritical flow), Equation (2.1) leads to two quantities, which are continuous across the jump. These are

$$[du] = 0 \quad \text{and} \quad \left[du^2 + \frac{1}{2}gd^2\right] = 0 \tag{2.7}$$

The first of these, together with Equation (2.2), implies that Q is constant throughout the domain for any steady flow, but from the second term and Equation (2.3), it is clear that there is a jump in H_{T} when the flow is discontinuous. Thus, the flow downstream of a stationary hydraulic jump is determined by the value of Q, which has been calculated for the transcritical upstream flow and the boundary condition specified at outflow.

Combining the two expressions (2.7) leads to a relationship between the branches of the solution on either side of the jump, given by

$$d_+ = \frac{d_-}{2}\left(\sqrt{1+8F_-^2} - 1\right) \tag{2.8}$$

in which d_+ is the depth immediately downstream of a discontinuity, while d_- and F_- are the depth and local Froude number immediately upstream. The flow sustains a stationary hydraulic jump if

$$(d_+)_{\text{out}} \leq d_{\text{out}} \leq d_{\text{in}} \tag{2.9}$$

where $(d_+)_{\text{out}}$ is calculated using Equation (2.8) together with the assumption that the jump occurs at the furthest downstream point of the constriction. Given the boundary conditions and the critical condition (which imply the values of Q and H_T), the solution on either side of the discontinuity can be calculated from Equation (2.4), so it only remains to find the point within the constriction at which condition (2.8) is satisfied. Both the upstream and downstream values of total head (H_{T_-} and H_{T_+} respectively) are known, and the upstream Froude number at the jump (F_-) can be found by solving iteratively

$$16(H_{T_-} - H_{T_+})(\sqrt{1+8F_-^2} - 1) - \frac{2H_{T_-}}{F_-^2 + 2}(\sqrt{1+8F_-^2} - 3)^3 = 0 \tag{2.10}$$

an equation which can be deduced from the jump conditions (2.7). The position of the jump is then found by combining Equation (2.10) with Equation (2.6).

It was noted earlier that an important point is the effect which the choice of physical boundary condition has on the solution. In numerical calculations a wide variety of conditions are applied; two of the most commonly used forms being

1. Q specified at subcritical inflow, d at subcritical outflow.
2. R^+ specified at subcritical inflow, R^- at subcritical outflow, where $R^{\pm} = u \pm 2\sqrt{gd}$ are the Riemann invariants of the homogeneous system.

At a supercritical inflow boundary all solution variables are specified, while nothing is specified at supercritical outflow. Note that the current discussion does not relate to the possible application of extra numerical boundary conditions, which are necessary for non-upwind numerical schemes.

Figure 1 illustrates the type of solution obtained using both sets of boundary conditions. Note its relationship with Figure 2, which was constructed in a similar manner for channel flows with variable bed topography instead of variable breadth. This is essentially figure 3 of Reference [7] but with the effect of boundary conditions taken into account. The main difference is the lack of a region where the channel becomes totally blocked (upstream of the obstacle d is less than the obstacle height and $u \equiv 0$) for type 1 boundary conditions, which the infinite channel allowed. Enforcing a specific value of Q at a subcritical inflow boundary ensures that the domain 'fills up' and a non-blocked ($u \neq 0$) steady state is reached. The flow parameters that have been specified in Figure 1 are $B_{\min}$, the minimum breadth of the channel (the shape of the channel need not be specified yet but it is assumed to vary continuously), and F_{in}, the 'initial' Froude number of the flow (the inflow Froude number proposed before any adjustments are made to Q and H_T due to the onset of transcritical flow). The latter, along with the condition that the 'initial' depth is given by $d_{\text{in}} = 1.0$, determine the values of the variables chosen to be prescribed at inflow and outflow boundaries (and also the initial

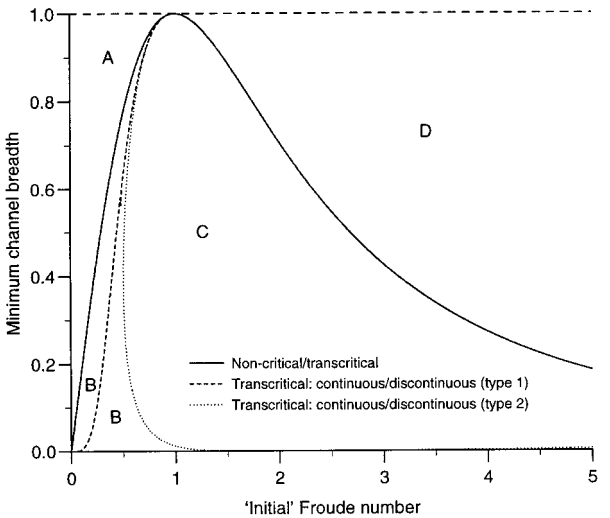

Figure 1. Types of exact solution to constricted channel flow test cases given different boundary conditions (varying breadth).

conditions required by the numerical schemes described later). The solid line in the figure indicates the transition between smooth flow, type A or D, and transcritical flow, type B or C, the broken/dotted lines represent the transition from discontinuous type B flow to smooth type C flow. Note that for supercritical 'initial' Froude numbers, these three curves coincide.

When F_{in} is subcritical the transition to transcritical flow is independent of the type of boundary conditions applied; however, particularly for the more severe channel constrictions, it is noticeable that type 2 boundary conditions are far more likely to sustain discontinuous flow. This difference in behaviour may well be due to the inhomogeneous nature of Equation (2.1), and the consequence that the Riemann invariants are not constant along characteristics. This suggests that type 1 boundary conditions should be used, simply to facilitate comparison with experiments, where Q and d are both measurable. The solutions depicted in Figure 3 confirm this. Although there is little difference to be seen between the depth profiles when $B_{\min} = 0.9$, the more extreme case shows very little resemblance between the solutions. Even though one would not expect an accurate prediction by the one-dimensional model for such a narrow constriction, this does not contradict the suggestion that type 1 boundary conditions should be used.

2.1. A one-dimensional numerical scheme

Equation (2.1) takes the general form

$$\underline{U}_t + \underline{F}_x = \underline{S} \tag{2.11}$$

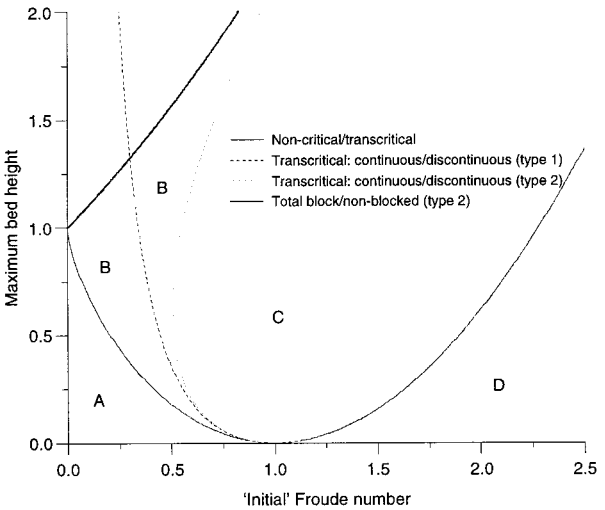

Figure 2. Types of exact solution to constricted channel flow test cases given different boundary conditions (varying bed).

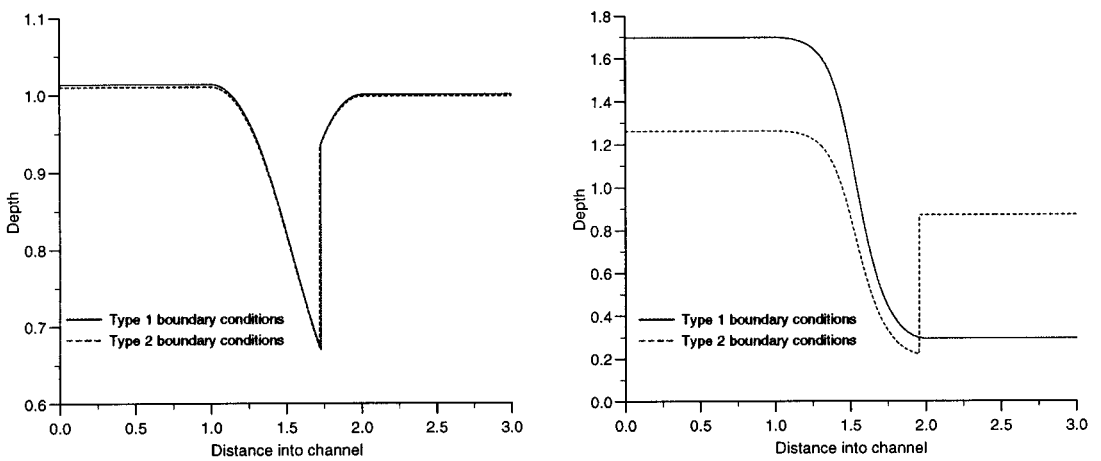

Figure 3. Exact solutions for different boundary conditions: $B_{\min} = 0.9$, $F_{\text{in}} = 0.67$ (left); $B_{\min} = 0.4$, $F_{\text{in}} = 0.5$ (right).

where $\underline{U}$ is the vector of conservative variables, $\underline{F}$ is the conservative flux vector (which varies with the channel breadth B independently of the conservative variables) and $\underline{S}$ represents the source terms.

A standard cell centre finite volume approximation is used for the flux terms in Equation (2.11) which, with forward Euler time stepping, gives

$$\underline{U}_i^{n+1} = \underline{U}_i^n - \frac{\Delta t}{\Delta x}(\underline{F}^*_{i+1/2} - \underline{F}^*_{i-1/2}) + \frac{\Delta t}{\Delta x}\underline{\mathbf{S}}^*_i \tag{2.12}$$

in which $\underline{F}^*$ represents a numerical flux evaluated at an interface between cells and $\underline{\mathbf{S}}^*$ is a numerical source integral over the cell.

Roe's scheme [8] is used here to discretize the flux derivatives, with a minor modification, described in more detail in Reference [9], which takes into account the dependence of the flux on the channel breadth $B(x)$. The flux difference across an interface (which occurs due to the discontinuous nature of the underlying representation of the solution) is split into independent components, giving

$$\Delta\underline{F}_{i+1/2} = (\tilde{\mathbf{A}}\Delta\underline{U} + \underline{\tilde{V}})_{i+1/2} = \left(\sum_{k=1}^{N_w} \tilde{\alpha}_k\tilde{\lambda}_k\underline{\tilde{r}}_k + \sum_{k=1}^{N_w}\tilde{\gamma}_k\underline{\tilde{r}}_k\right)_{i+1/2} \tag{2.13}$$

where $\underline{\tilde{V}} \approx (\partial\underline{F}/\partial B)\Delta B$. $\Delta\underline{F}$ represents the jump in $\underline{F}$ across the edge of a grid cell, $\underline{\tilde{r}}_k$ are the right eigenvectors of $\tilde{\mathbf{A}} \approx \partial\underline{F}/\partial\underline{U}$, the approximate flux Jacobian, $\tilde{\lambda}_k$ are the eigenvalues of $\tilde{\mathbf{A}}$, and $\tilde{\alpha}_k$ are the 'strengths' associated with each component of the decomposition. Additionally, $\tilde{\gamma}_k$ are the coefficients of the decomposition of the extra term $\underline{\tilde{V}}$ on to the eigenvectors of $\tilde{\mathbf{A}}$ and $N_w = 2$ is the number of equations in system (2.11). Throughout, $\tilde{\cdot}$ denotes the evaluation of a quantity at its Roe-average state [8], defined specifically so that Equation (2.13) is satisfied.

In the case considered here, that of one-dimensional shallow water flows through a channel of varying breadth, the decomposition is completely defined by

$$\tilde{\alpha}_1 = \frac{\Delta(Bd)}{2} + \frac{1}{2\tilde{c}}(\Delta(Bdu) - \tilde{u}\Delta(Bd)), \qquad \tilde{\alpha}_2 = \frac{\Delta(Bd)}{2} - \frac{1}{2\tilde{c}}(\Delta(Bdu) - \tilde{u}\Delta(Bd))$$

$$\tilde{\lambda}_1 = \tilde{u} + \tilde{c}, \qquad \tilde{\lambda}_2 = \tilde{u} - \tilde{c}, \qquad \tilde{\gamma}_1 = -\frac{1}{4g}\tilde{c}^3\Delta B, \qquad \tilde{\gamma}_2 = \frac{1}{4g}\tilde{c}^3\Delta B$$

$$\underline{\tilde{r}}_1 = \begin{pmatrix} 1 \\ \tilde{u} + \tilde{c} \end{pmatrix}, \qquad \underline{\tilde{r}}_2 = \begin{pmatrix} 1 \\ \tilde{u} - \tilde{c} \end{pmatrix} \tag{2.14}$$

where $c = \sqrt{gd}$ is the local wave celerity, and

$$\tilde{u} = \overline{\sqrt{Bdu}}/\overline{\sqrt{Bd}} \quad \text{and} \quad \tilde{c}^2 = g\overline{\sqrt{Bd}}/\overline{\sqrt{B}} \tag{2.15}$$

in which $\bar{\cdot}$ is the arithmetic mean of the values on either side of the interface across which the flux difference is being taken.

The numerical fluxes used in Equation (2.12) are

$$\underline{F}^{*}_{i+1/2} = \frac{1}{2}(\underline{F}^{\mathrm{R}}_{i+1/2} + \underline{F}^{\mathrm{L}}_{i+1/2}) - \frac{1}{2}\left(\sum_{k=1}^{N_w} \tilde{\alpha}_k |\tilde{\lambda}_k| \tilde{\underline{r}}_k + \sum_{k=1}^{N_w} \tilde{\gamma}_k \operatorname{sgn}(\tilde{\lambda}_k)\tilde{\underline{r}}_k\right)_{i+1/2} \tag{2.16}$$

which gives a high resolution MUSCL-type algorithm [10] when the superscripts 'R' and 'L' represent evaluation on the right- and left-hand sides respectively of the interface; the Roe averages $\tilde{\cdot}$ are now calculated from a limited linear reconstruction of the solution. The reconstruction stage is carried out here using the minmod limiter [11].

As described in detail in Reference [9], the approximate source term integral associated with an interface between cells can similarly be projected onto the eigenvectors of the flux Jacobian so that, in its linearized form, it becomes

$$\int_{x_i}^{x_{i+1}} \underline{S}\, \mathrm{d}x \approx \tilde{\underline{\mathbf{S}}}_{i+1/2} = \left(\sum_{k=1}^{N_w} \tilde{\beta}_k \tilde{\underline{r}}_k\right)_{i+1/2} \tag{2.17}$$

where $\tilde{\beta}_k$ are the coefficients of the decomposition on to the eigenvectors of $\tilde{\mathbf{A}}$. For Equation (2.1) this leads to

$$\tilde{\beta}_1 = \frac{1}{4g}\tilde{c}_3 \Delta b = -\tilde{\beta}_2 \tag{2.18}$$

The numerical source term integral of Equation (2.1) is approximated by

$$\underline{\mathbf{S}}^{*}_i = (\tilde{\underline{\mathbf{S}}}^{-}_{i+1/2} + \tilde{\underline{\mathbf{S}}}^{+}_{i-1/2}) - \tilde{\underline{\mathbf{S}}}(\underline{U}^{\mathrm{L}}_{i+1/2}, \underline{U}^{\mathrm{R}}_{i-1/2}) \tag{2.19}$$

in which the edge contributions are given by

$$\tilde{\underline{\mathbf{S}}}^{-}_{i+1/2} = \frac{1}{2}\left(\sum_{k=1}^{N_w} \tilde{\beta}_k (1 - \operatorname{sgn}(\tilde{\lambda}_k))\tilde{\underline{r}}_k\right)_{i+1/2}, \qquad \tilde{\underline{\mathbf{S}}}^{+}_{i-1/2} = \frac{1}{2}\left(\sum_{k=1}^{N_w} \tilde{\beta}_k (1 + \operatorname{sgn}(\tilde{\lambda}_k))\tilde{\underline{r}}_k\right)_{i-1/2} \tag{2.20}$$

which are evaluated, like the flux differences, from the interface values that arise from the limited linear reconstruction of the solution within each cell. The second term in Equation (2.19), $\tilde{\underline{\mathbf{S}}}(\cdot, \cdot)$, is simply the source term integral approximated over the mesh cell and hence evaluated at the Roe average of the left and right states of the linear reconstruction of the solution within that cell. The standard Courant–Friedrich–Lewy (CFL) limit, given by

$$\max_k(\tilde{\lambda}_k)\frac{\Delta t}{\Delta x} \leq 1 \tag{2.21}$$

is used to obtain a stable time step for the scheme.

3. THE TWO-DIMENSIONAL MODEL

In two dimensions, the shallow water equations in conservative form are given by

$$\underline{U}_t + \underline{F}_x + \underline{G}_y = \underline{0} \tag{3.1}$$

where

$$\underline{U} = \begin{pmatrix} d \\ du \\ dv \end{pmatrix}, \qquad \underline{F} = \begin{pmatrix} du \\ du^2 + \frac{1}{2} g d^2 \\ duv \end{pmatrix}, \qquad \underline{G} = \begin{pmatrix} dv \\ duv \\ dv^2 + \frac{1}{2} g d^2 \end{pmatrix} \tag{3.2}$$

in which d is the depth of the flow, u and v are the x and y velocities of the flow respectively, and g is the acceleration due to gravity. The effects of the varying breadth of the channel are applied solely by the shape of the domain over which these equations are solved and the boundary conditions that are applied there; so unlike the one-dimensional model these equations have no source terms. The boundary condition applied at the solid walls of the channel simply enforces zero mass flux through the wall ($\vec{u} \cdot \vec{n} = 0$, where $\vec{u}$ is the flow velocity and $\vec{n}$ is a boundary normal).

3.1. A two-dimensional numerical scheme

A multi-dimensional upwind fluctuation distribution scheme has been used here to solve Equation (3.1) on unstructured triangular meshes. It is based on the method developed by Mesaros and Roe [12] for the solution of the Euler equations and is described in detail in Reference [13].

The scheme is composed of two stages: a distribution step, described briefly later, and a decomposition step, in which the flux balance

$$\underline{\Phi} = \iint_{\triangle} \underline{U}_t \, \mathrm{d}x \, \mathrm{d}y = -\iint_{\triangle} (\underline{F}_x + \underline{G}_y) \, \mathrm{d}x \, \mathrm{d}y = \oint_{\partial \triangle} (\underline{F}, \underline{G}) \cdot \mathrm{d}\vec{n} \tag{3.3}$$

where $\vec{n}$ is an inward pointing normal to the boundary $\partial \triangle$ of the triangular cell, is linearized and split into simpler components. The linearization is constructed so that the discrete flux balance can be written

$$\tilde{\underline{\Phi}} = -S_{\triangle}(\mathbf{A}\underline{U}_x + \mathbf{B}\underline{U}_y)|_{\tilde{Z}} = -S_{\triangle}(\tilde{\mathbf{A}}, \tilde{\mathbf{B}}) \cdot \vec{\nabla} \underline{U} \tag{3.4}$$

where $\mathbf{A} = \partial \underline{F} / \partial \underline{U}$ and $\mathbf{B} = \partial \underline{G} / \partial \underline{U}$ are the flux Jacobian matrices and $S_{\triangle}$ is the area of the triangular cell. This is carried out so that the system can be decomposed without losing the conservative nature of the scheme. Here

$$\underline{Z} = (d, u, v)^T \tag{3.5}$$

is chosen, and a small correction in the form of a source term, which can also be distributed, is added for conservation [13]. For the purposes of simplicity, the notation $\tilde{\cdot}$, which once again represents a linearized quantity in Equation (3.1), is implicit in each expression from now on.

The decomposition is carried out by attempting to diagonalize a preconditioned form of the original system of equations (3.1). The resulting flux balance takes the form

$$\underline{\Phi} = \sum_{k=1}^{N_w} \phi^k \underline{r}^k \tag{3.6}$$

a sum of N_w much simpler components or waves, each corresponding to a fluctuation ϕ^k and which can be discretized individually in a straightforward manner. In Equation (3.6), $\underline{r}^k$ are the columns of the matrix

$$\mathbf{R} = \frac{\partial \underline{U}}{\partial \underline{Q}} \mathbf{P}^{-1} \frac{\partial \underline{Q}}{\partial \underline{W}}$$

in which $\mathbf{P}$ is the chosen preconditioning matrix. $\underline{Q}$ is an intermediate set of (symmetrizing) variables, given by

$$\partial \underline{Q} = \left(\sqrt{\frac{g}{d}} \partial d, \partial q, q\, \partial \theta \right)^T \tag{3.7}$$

where $q = \sqrt{u^2 + v^2}$ is the flow speed and $\theta = \tan^{-1}(v/u)$ is the direction of the flow and introduced purely to simplify the algebra. The system is also transformed into streamwise co-ordinates, ξ and η, which further simplify the situation. $\underline{W}$ is the vector of 'characteristic' variables, giving the partially diagonalized system

$$\underline{W}_t + \mathbf{A}_W \underline{W}_\xi + \mathbf{B}_W \underline{W}_\eta = \underline{0} \tag{3.8}$$

in which $\mathbf{A}_W$ and $\mathbf{B}_W$ are the Jacobian matrices with respect to the variables $\underline{W}$. A fluctuation distribution scheme is applied to each of the components of Equation (3.8) and the corresponding distribution of the conservative flux balance is then recovered from this via the transformation back to the original system (multiplication by $\mathbf{R}$). A careful choice of $\mathbf{P}$ gives an optimal decoupling of system (3.8); complete in supercritical flow, but unavoidably including a coupled 2×2 elliptic subsystem for subcritical flow.

The preconditioner of Mesaros and Roe [12] modifies straightforwardly to a form that can be used with the shallow water equations [13], giving

$$\mathbf{P} = \frac{1}{q}\begin{pmatrix} \dfrac{\varepsilon F^2}{\beta\kappa} & -\dfrac{\varepsilon F}{\beta\kappa} & 0 \\ -\dfrac{\varepsilon F}{\beta\kappa} & \dfrac{\varepsilon}{\beta\kappa}+\varepsilon & 0 \\ 0 & 0 & \dfrac{\beta}{\kappa} \end{pmatrix} \tag{3.9}$$

where $F = q/\sqrt{gd}$ is the local Froude number of the flow

$$\beta = \sqrt{|F^2 - 1|}\,, \qquad \kappa = \max(F, 1) \tag{3.10}$$

and $\varepsilon = \varepsilon(F)$ is a function that satisfies $\varepsilon(0) = \frac{1}{2}$ and $\varepsilon(F) = 1$ for $F \geq 1$ (giving the correct behaviour in the preconditioned system at stagnation and continuity of the optimal decomposition through the critical point), and is taken here to be

$$\varepsilon(F) = \begin{cases} -F^3 + \dfrac{3}{2}F^2 + \dfrac{1}{2} & \text{for } 0 \leq F \leq 1 \\ 1 & \text{for } F > 1 \end{cases} \tag{3.11}$$

Two different forms for the characteristic variables $\underline{W}$ are taken, depending on whether the flow is supercritical or subcritical. These are given by

$$\partial \underline{W}_{\text{sup}} = \begin{pmatrix} \sqrt{\dfrac{g}{d}}\,\beta\,\partial d + Fq\,\partial\theta \\ \sqrt{\dfrac{g}{d}}\,\beta\,\partial d - Fq\,\partial\theta \\ \sqrt{\dfrac{g}{d}}\,\partial d + F\,\partial q \end{pmatrix}, \qquad \partial \underline{W}_{\text{sub}} = \begin{pmatrix} \dfrac{\beta g}{q}\,\partial d \\ q\,\partial\theta \\ \sqrt{\dfrac{g}{d}}\,\partial d + F\,\partial q \end{pmatrix} \tag{3.12}$$

respectively, and this choice gives a continuous representation through the critical point. In supercritical flow this leads to characteristic Jacobians in Equation (3.8) of the form

$$\mathbf{A}_W = \begin{pmatrix} \dfrac{\beta}{\kappa} & 0 & 0 \\ 0 & \dfrac{\beta}{\kappa} & 0 \\ 0 & 0 & 1 \end{pmatrix}, \qquad \mathbf{B}_W = \begin{pmatrix} \dfrac{1}{\kappa} & 0 & 0 \\ 0 & \dfrac{1}{\kappa} & 0 \\ 0 & 0 & 0 \end{pmatrix} \tag{3.13}$$

the system is fully decoupled and each component can be treated as a scalar advection equation. In subcritical flow

$$\mathbf{A}_W = \begin{pmatrix} -\varepsilon\beta & 0 & 0 \\ 0 & \beta & 0 \\ 0 & 0 & \varepsilon \end{pmatrix}, \qquad \mathbf{B}_W = \begin{pmatrix} 0 & \varepsilon & 0 \\ 1 & 0 & 0 \\ 0 & 0 & 0 \end{pmatrix} \tag{3.14}$$

which contains a coupled 2×2 subsystem.

For the completely decoupled components, the associated scalar fluctuation

$$\phi = -S_{\triangle}(\vec{\lambda}\cdot\vec{\nabla}W) \tag{3.15}$$

where $\vec{\lambda}$ is the advection velocity for the wave and is distributed using an upwind fluctuation distribution scheme. If explicit forward Euler time stepping is used, this leads to a nodal update of the form

$$u_i^{n+1} = u_i^n + \frac{\Delta t}{S_i} \sum_{j \in \cup \triangle_i} \alpha_i^j \phi_j \tag{3.16}$$

where S_i is the area of the median dual cell for node i (one third of the total area of the triangles with a vertex at i), α_i^j is the distribution coefficient that indicates the proportion of the fluctuation ϕ_j to be sent from cell j to node i (not to be confused with the wave strengths it represents in Section 2.1), and $\cup \triangle_i$ represents the set of cells adjacent to node i.

Each wave in each triangle is considered individually. For a given wave, any triangle with only one downstream vertex (a vertex for which $\vec{\lambda}\cdot\vec{n} > 0$, $\vec{n}$ being an inward pointing normal to the opposite edge) sends the whole of its fluctuation to that grid node. For a cell with two inflow sides (choosing here, without loss of generality, vertices 1 and 2 to be the downstream nodes) considered in isolation, the N scheme [14] contributions are

$$\begin{aligned} S_1 u_1 &\to S_1 u_1 - \Delta t k_1 (u_1 - u_3) \\ S_2 u_2 &\to S_2 u_2 - \Delta t k_2 (u_2 - u_3) \\ S_3 u_3 &\to S_3 u_3 \end{aligned} \tag{3.17}$$

where $k_l = \frac{1}{2}\vec{\lambda}\cdot\vec{n}_l$ ($\vec{n}$ is now scaled by the edge length). This scheme is positive and therefore stable for a restriction on the time step at a node i, given by

$$\Delta t \leq \frac{S_i}{\sum_{j \in \cup \triangle_i} \max(0, k_i^j)} \tag{3.18}$$

A linearity preserving scheme (second-order accurate at the steady state) is obtained from the N scheme by replacing the overall contributions

$$\psi_1 = -k_1(u_1^n - u_3^n), \qquad \psi_2 = -k_2(u_2^n - u_3^n) \tag{3.19}$$

to the downstream nodes in the two-target case by 'limited' contributions

$$\psi_1^* = \psi_1 - L(\psi_1, -\psi_2), \qquad \psi_2^* = \psi_2 - L(\psi_2, -\psi_1) \tag{3.20}$$

$L(x, y)$ can be any member of the family of symmetric limiter functions, although the minmod limiter [11] is the only one for which the 'limited' scheme remains positive. The resulting method is the positive streamwise invariant (PSI) scheme [14], used here for the distribution of scalar fluctuations.

The elliptic subsystem, when it appears, is distributed using a Lax–Wendroff scheme with 2×2 matrix distribution coefficients

$$\boldsymbol{\alpha}_i^j = \frac{1}{3}\mathbf{I} + \frac{\Delta t}{4S_{\triangle_j}}(\mathbf{A}, \mathbf{B})_j \cdot \vec{n}_i^j \tag{3.21}$$

The overall scheme used to solve Equation (3.1) takes the form

$$\underline{U}_i^{n+1} = \underline{U}_i^n + \frac{\Delta t}{S_i} \sum_{j \in \cup \triangle_i} ((\underline{r}_j^1, \underline{r}_j^2)\boldsymbol{\alpha}_i^j \boldsymbol{\phi}_j + (\alpha_i^j)^3 \phi_j^3 \underline{r}_j^3) \tag{3.22}$$

in subcritical flow, and contains one scalar component and one subsystem, with corresponding vector fluctuation $\boldsymbol{\phi}_j$. More simply

$$\underline{U}_i^{n+1} = \underline{U}_i^n + \frac{\Delta t}{S_i} \sum_{j \in \cup \triangle_i} \left(\sum_{k=1}^{3} (\alpha_i^j)^k \phi_j^k \underline{r}_j^k \right) \tag{3.23}$$

in the supercritical case.

4. NUMERICAL RESULTS

For the purposes of this comparison, each of the results presented is for a channel of length 3 units, which has a symmetric constriction of length 1 unit at its centre and whose breadth is given by

$$B(x) = \begin{cases} 1 - (1 - B_{\min}) \cos^2(\pi(x - 1.5)) & \text{for } |x - 1.5| \le 0.5 \\ 1 & \text{otherwise} \end{cases} \tag{4.1}$$

where $B_{\min}$ is the minimum channel breadth and x is the distance into the channel (so the throat is positioned at the midpoint of the constriction). In the two-dimensional case, the constriction has been chosen for simplicity to be represented by symmetric indentations on either side of the channel (as illustrated in Figure 9). While alternative constrictions undoubtedly alter the flow in some way, their effect on the qualitative comparison with one-dimensional results is not significant.

Each of the one-dimensional numerical solutions is obtained on a uniform 76-node grid, giving comparable resolution to the two-dimensional grids used, each of which has been constructed using a simple advancing front technique (see, for example, Reference [15]) with an underlying mesh spacing parameter of 0.04. The initial conditions for each numerical experiment (in which the steady state solution is achieved by approximating the evolution of the time-dependent shallow water equations (2.1) with steady boundary conditions and converging to the steady state from the initial conditions as $t \to \infty$) were $d = 1.0$ and $F = F_{\text{in}}$, with $v = 0.0$ in two dimensions.

Figure 4 shows how well the one-dimensional numerical results agree with the theory (as illustrated in Figure 1) in terms of the parameter values ($B_{\min}$ and F_{in}) at which transition occurs between the different types of steady solution obtained. Different symbols have been used to indicate the types of solution (A–D) predicted by the numerical scheme. Regions of the graph have been left empty, but the solution type is implied by the symbol on the boundary of the region. It is interesting to note that with many commonly used approximations to the source terms, such as a simple pointwise evaluation, the agreement with theory is less close. In some cases they can predict unphysical phenomena, such as a continuous steady state, which is supercritical at both inflow and outflow but has a subcritical region around the throat of the channel.

The corresponding two-dimensional numerical results are shown in Figure 5. In this case, type 1 boundary conditions correspond to specifying du and setting $v = 0$ at subcritical inflow and d at subcritical outflow; type 2 boundary conditions being where $R^+ = u + 2\sqrt{gd}$ and $v = 0$ are specified at subcritical inflow and $R^- = u - 2\sqrt{gd}$ is given at subcritical outflow (where it has been assumed that these boundaries are parallel to the y-axis). It is immediately clear that the multi-dimensional nature of the geometry has a significant effect on the solution,

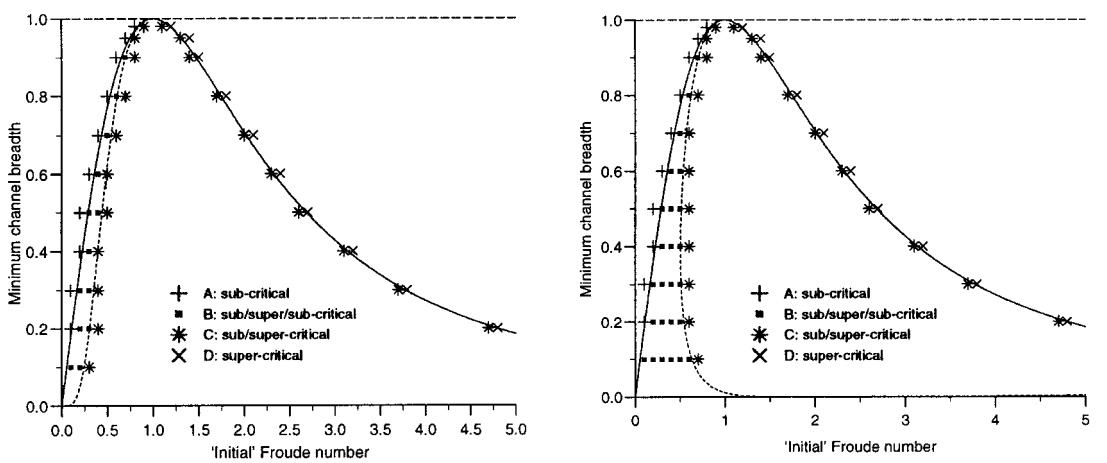

Figure 4. Types of one-dimensional numerical solution to constricted channel flow test cases with boundary conditions of type 1 (left) and type 2 (right).

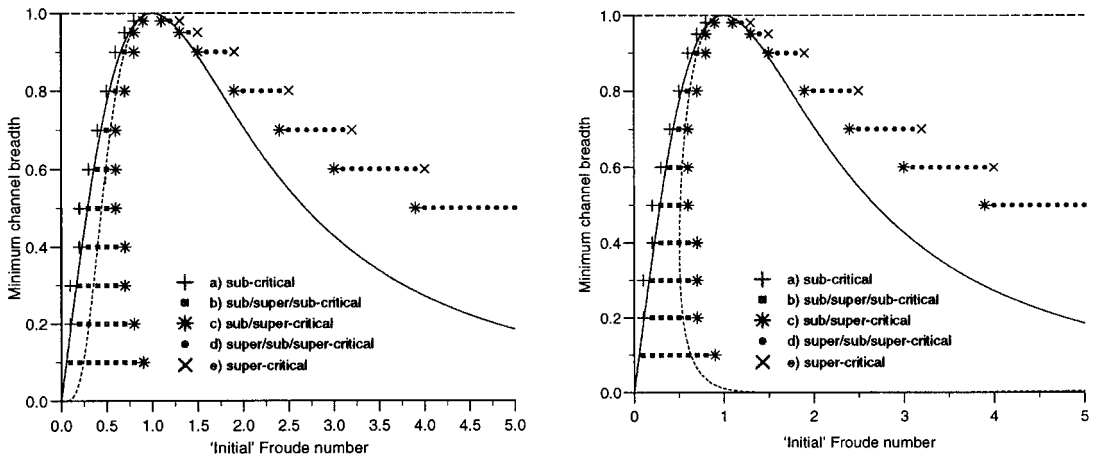

Figure 5. Types of two-dimensional numerical solution to constricted channel flow test cases with boundary conditions of type 1 (left) and type 2 (right).

the differences occurring whenever the two-dimensional flow is not smooth. This includes every steady state that has some supercritical component (compare with Figure 9). As expected, the more narrow the constriction, the greater the effect, but even the smallest indentation allows a steady state solution that is supercritical at both inflow and outflow but has a subcritical pocket within the constriction.

Including the two-dimensional results shows that now five different types of solution may occur

(a) Smooth and purely subcritical.
(b) Subcritical at inflow and outflow, critical at the channel throat, with a steady discontinuity in the diverging region of the channel.
(c) Smooth (apart from the oblique downstream jumps in two dimensions), subcritical at inflow, critical at the throat, and supercritical at outflow.
(d) Smooth in one dimension, supercritical at inflow and outflow, with oblique jumps and a subcritical region in the constriction for two-dimensional flow.
(e) Smooth in one dimension and purely supercritical in every case.

This corresponds to the one-dimensional situation, with the addition that case D of Section 2 has now split into two cases, (d) and (e).

Interestingly, the type of solution generated in two dimensions no longer depends to any great extent on the type of boundary condition employed. (There is only one difference between the two graphs of the numerical results in Figure 5, at $B_{\min} = 0.2$, $F_{\text{in}} = 0.7$.) This close resemblance seems to be due to the fact that, unlike the one-dimensional system, the two-dimensional equations are homogeneous. Quantitatively though, there is still a considerable difference between the corresponding steady state solutions, particularly in the more

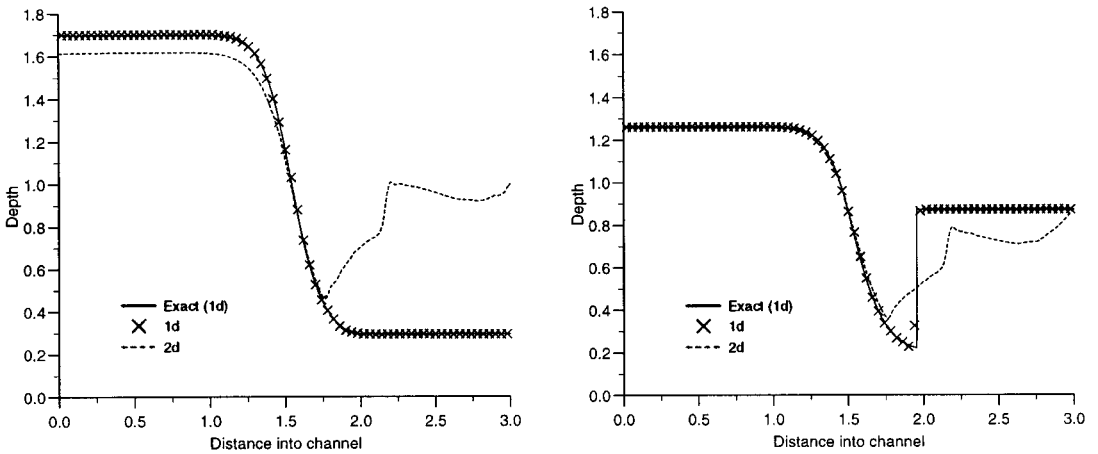

Figure 6. Comparison of depth for $B_{\min} = 0.4$ and $F_{\text{in}} = 0.5$ with boundary conditions of type 1 (left) and type 2 (right).

extreme cases. This is illustrated in Figure 6 in which analytical and numerical solutions to the one-dimensional equations are compared with breadth-averaged numerical solution values obtained in two dimensions. The depth contours shown in Figure 7 for type 2 boundary conditions illustrate the two-dimensional nature of the highly curved hydraulic jump in this case.

It is also clear in this case that the essentially one-dimensional nature of the downstream boundary condition (a single value of R^- is imposed over the whole length of the outflow boundary) is inadequate here; the downstream boundary is too close and the combination of subcritical flow and genuine two-dimensional variations in the solution here contaminates the approximation within the domain and hinders convergence to the steady state (since one does not exist for the imposed boundary condition). In this simple case, the problem is alleviated by moving the outflow boundary further downstream, but only at significant computational expense. For type 1 boundary conditions there is also a noticeable difference at inflow between

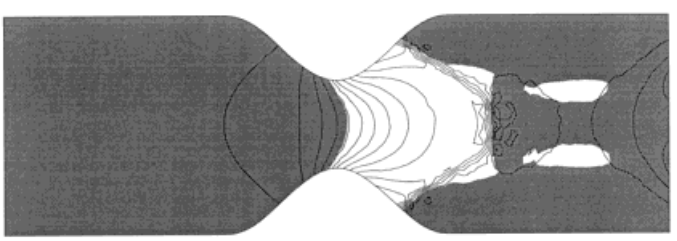

Figure 7. Depth contours for $B_{\min} = 0.4$ and $F_{\text{in}} = 0.5$.

the one- and two-dimensional solutions, for similar reasons and with the same remedy. The advantages of using type 1 boundary conditions are retained from one dimension, but there is a stronger argument for using type 2 boundary conditions in two dimensions since they are considerably more robust when the transverse variation of the solution is not accounted for at the boundary.

Figure 8 shows an example of each of the five different types of solution obtained for a less extreme channel geometry using type 1 boundary conditions. The corresponding contour plots of depth for the two-dimensional solutions are shown in Figure 9 (subcritical regions have been shaded to distinguish them). The same cases are shown in Figure 10, this time using a standard MUSCL-type cell centre finite volume scheme for unstructured triangular meshes. The scheme used is the Limited Central Difference (LCD) scheme of Liu [16] and the results are generally very similar, although they exhibit more numerical diffusion, illustrated by the slight asymmetry in the subcritical test case and all discontinuities being captured slightly less sharply. The only significant difference is in the second, transcritical case ($F_{\text{in}} = 0.67$), where the extra diffusion has caused the hydraulic jump to almost disappear: here the multi-dimensional upwind scheme shows its advantage.

In order to illustrate the conservative nature of the numerical schemes, profiles of discharge Q along the channel are plotted in Figure 11. Except for some small perturbations close to discontinuities, the numerical schemes maintain the correct constant value of Q throughout the channel in each case.

The discrepancies that can be seen in Figure 8 between the one-dimensional exact and numerical results (which are in close agreement) and the two-dimensional breadth-averaged results at the higher Froude numbers can be clearly related to the appearance of oblique discontinuities (undular jumps), genuine multi-dimensional features of the solution which are triggered by the constriction when the flow becomes supercritical at outflow. Note that once the flows become completely supercritical the agreement between the one- and two-dimensional results gradually improves as the flow speed increases because the jumps become parallel to the flow direction. The influence of the oblique discontinuities on supercritical flow is illustrated even more dramatically in Figures 12 and 13, which depict the depth of the flow for a channel with a quadruple symmetric constriction with $B_{\text{min}} = 0.9$ and $F_{\text{in}} = 1.9$. The one-dimensional model predicts smooth supercritical flow throughout, but the comparison with two dimensions becomes progressively worse as the jumps interact with each other.

5. CONCLUSIONS

In this work a comparison has been made between one- and two-dimensional models of steady state shallow water flow through an open channel of varying breadth using numerical methods developed recently for the solution of the shallow water equations [9,13]. It has been shown that the numerical and analytical solutions to the one-dimensional model agree closely, provided that an appropriate discretization of the source terms is employed.

When the flow is completely smooth and subcritical, these solutions also prove to be an accurate prediction of the breadth-averaged two-dimensional flow. For small constrictions ($B_x \ll 1$) the agreement remains good even when the one-dimensional model predicts a

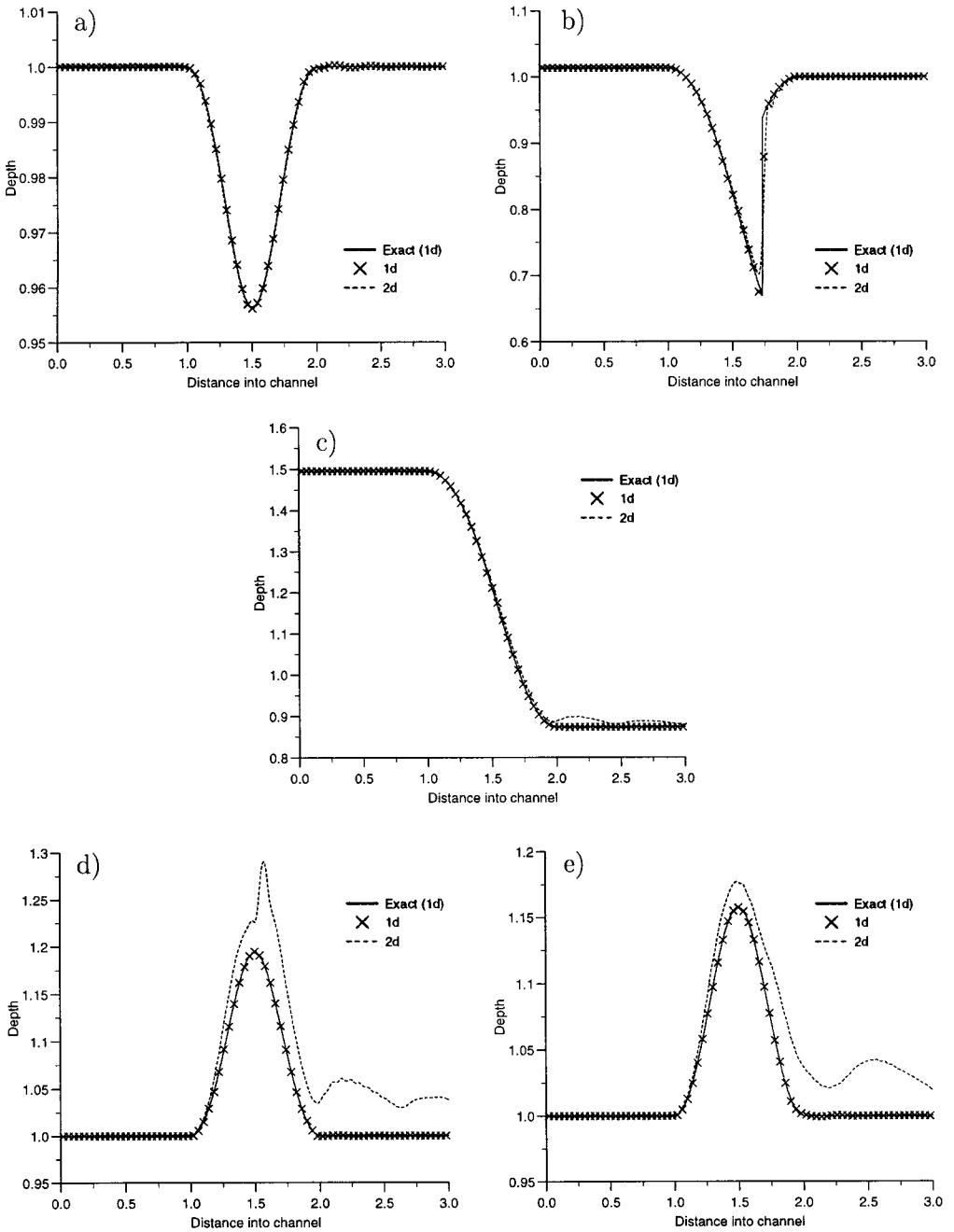

Figure 8. Comparison of depth for $B_{\min} = 0.9$ with initial Froude numbers F_{in} of (a) 0.5, (b) 0.67, (c) 1.2, (d) 1.7 and (e) 2.0.

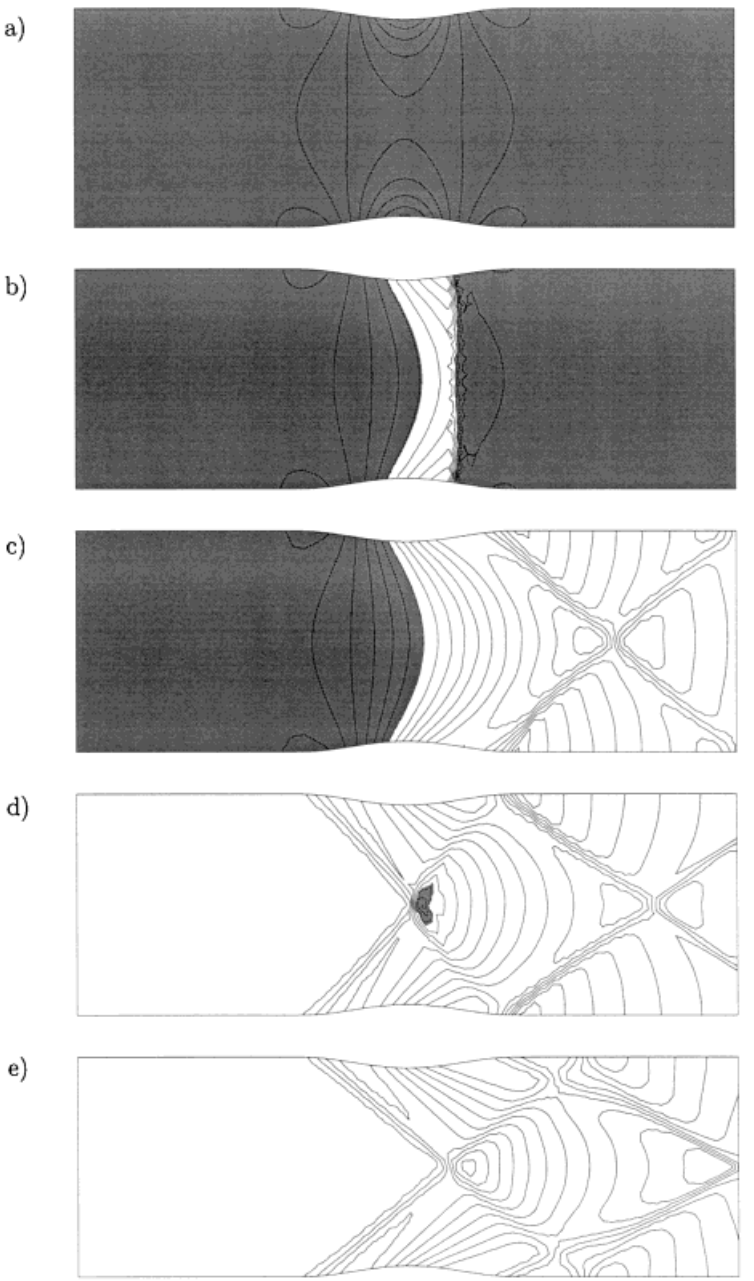

Figure 9. Depth contours for $B_{\min} = 0.9$ with initial Froude numbers F_{in} of (a) 0.5, (b) 0.67, (c) 1.2, (d) 1.7 and (e) 2.0 (multi-dimensional upwind scheme).

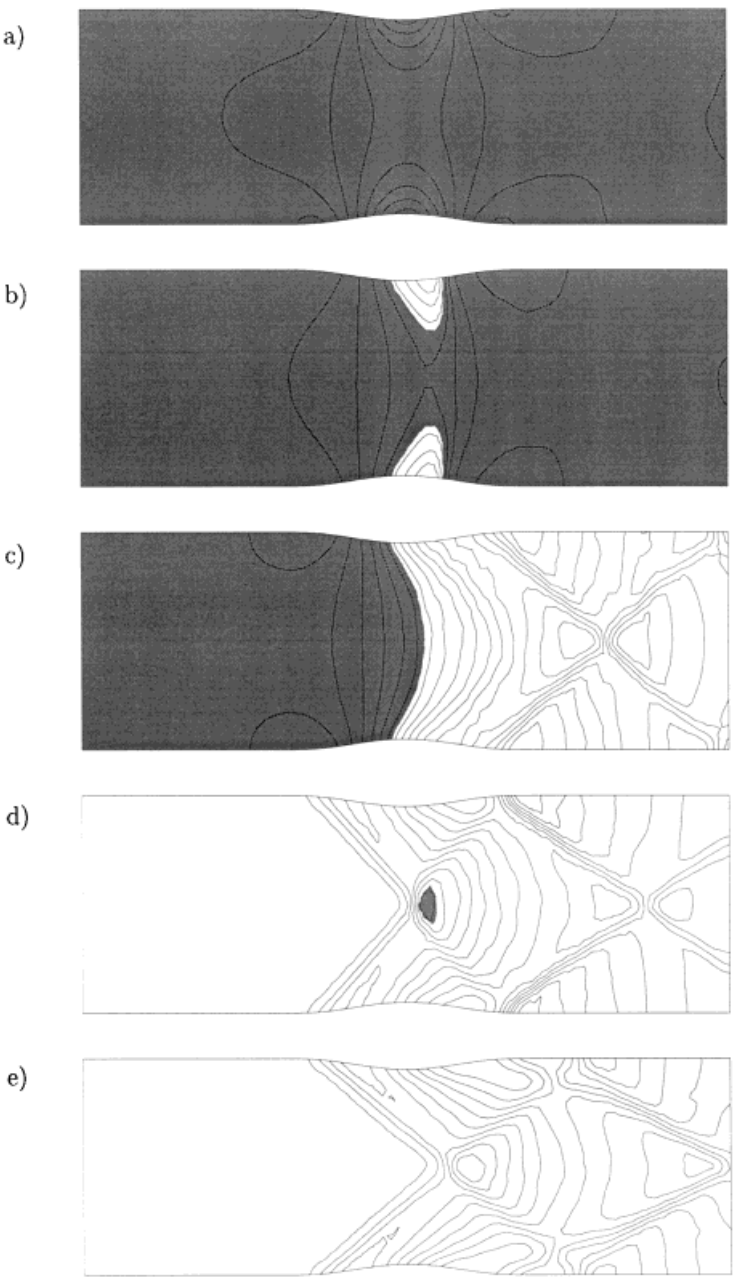

Figure 10. Depth contours for $B_{\min} = 0.9$ with initial Froude numbers F_{in} of (a) 0.5, (b) 0.67, (c) 1.2, (d) 1.7 and (e) 2.0 (MUSCL-type finite volume scheme).

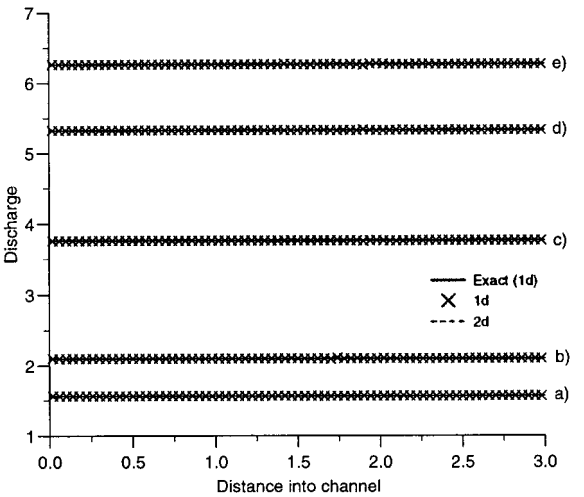

Figure 11. Comparison of discharge for $B_{\min} = 0.9$ with initial Froude numbers F_{in} of (a) 0.5, (b) 0.67, (c) 1.2, (d) 1.7 and (e) 2.0.

discontinuous flow, because the transverse acceleration in the flow is negligible and consequently the two-dimensional solution remains essentially one-dimensional. As the constriction narrows, however, steady hydraulic jumps become more curved and the one-dimensional model less accurate. When the flow downstream of the constriction is supercritical, the undular jumps that are propagated from the constriction in the two-dimensional case cannot be

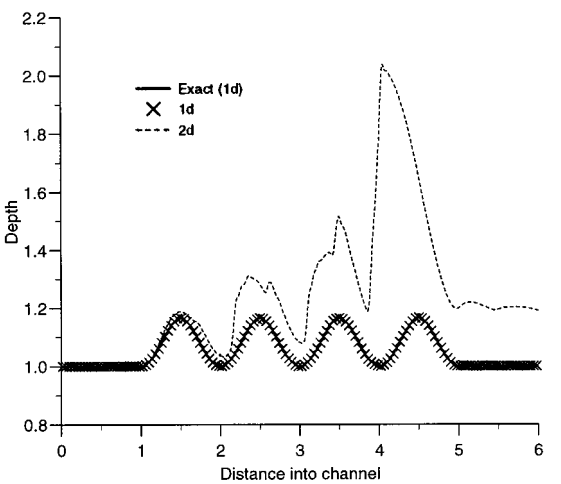

Figure 12. Comparison of depth for the quadruple constriction test case with $B_{\min} = 0.9$ and $F_{\text{in}} = 1.9$.

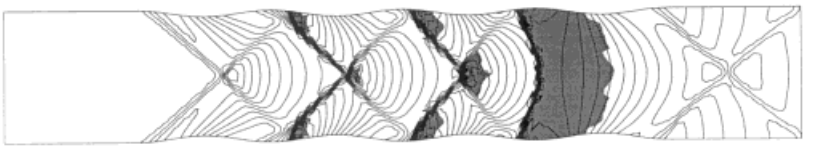

Figure 13. Depth contours for the quadruple constriction test case with $B_{\min} = 0.9$ and $F_{\text{in}} = 1.9$.

predicted by the one-dimensional equations and the accuracy of the simpler model is poor, even for channels with relatively small indentations which should satisfy the assumptions under which the one-dimensional model is derived. The agreement does, however, become closer again as the speed of the flow increases and these discontinuities become aligned with the channel.

Two commonly used forms of boundary condition have been compared, and it has been shown that when the flow is transcritical they can give widely differing solutions for given geometries and initial flow parameters. In one dimension, specifying discharge at inflow and depth at outflow seems appropriate since both their values can be determined simply from experiment. In two dimensions, however, when the equations are homogeneous, specifying Riemann invariants proves to be more robust. In both cases though, the inadequacy of applying a condition along a boundary uniformly when the flow is subcritical is highlighted, unless the boundary is positioned far enough away from the obstacle.

ACKNOWLEDGMENTS

The author would like to thank Dr D. Porter and Professor M.J. Baines for their contributions to this work, Dr I. MacDonald for the use of his one-dimensional code, and the EPSRC for providing the funding for the author under grant number GK/K74616.

REFERENCES

1. Johnson RS. *A Modern Introduction to the Mathematical Theory of Water Waves*. Cambridge University Press: Cambridge, 1997.
2. Stoker JJ. *Water Waves: The Mathematical Theory with Applications*. Interscience: New York, 1958.
3. Cunge JA, Holly FM, Verwey A. *Practical Aspects of Computational River Hydraulics*. Pitman: London, 1980.
4. MacDonald I, Baines MJ, Nichols NK, Samuels PG. Analytic benchmark solutions for open-channel flows. *Journal of Hydraulic Engineering ASCE* 1997; **123**(11): 1041–1045.
5. Alcrudo F. Esquemas de Alta Resolucion de Variacion Total Decreciente para el Estudio de Flujos Discontinuos de Superficie Libre. PhD thesis, University of Zaragoza, 1992.
6. Broad AS, Porter D, Sewell MJ. New shallow flows over an obstacle. *Quarterly Journal of Mechanics and Applied Mathematics* 1997; **50**(4): 625–653.
7. Houghton DD, Kasahara A. Nonlinear shallow fluid flow over an isolated ridge. *Communications in Pure and Applied Mathematics* 1968; **21**: 1–23.
8. Roe PL. Approximate Riemann solvers, parameter vectors, and difference schemes. *Journal of Computational Physics* 1981; **43**(2): 357–372.
9. Hubbard ME, Garcia-Navarro P. Flux difference splitting and the balancing of source terms and flux gradients. *Journal of Computational Physics* 2000; **165**(1): 89–125.

10. van Leer B. Towards the ultimate conservative difference scheme V. A second order sequel to Godunov's method. *Journal of Computational Physics* 1979; **32**: 101–136.
11. Sweby PK. High resolution schemes using flux limiters for hyperbolic conservation laws. *SIAM Journal of Numerical Analysis* 1984; **21**: 995–1011.
12. Mesaros LM, Roe PL. Multidimensional fluctuation-splitting schemes based on decomposition methods. AIAA Paper 95-1699, AIAA CFD Conference AIAA CP-956, 1995.
13. Hubbard ME, Baines MJ. Conservative multidimensional upwinding for the steady two-dimensional shallow water equations. *Journal of Computational Physics* 1997; **138**: 419–448.
14. Deconinck H, Struijs R, Bourgois G, Roe PL. High resolution shock capturing cell vertex advection schemes for unstructured grids. In *Computational Fluid Dynamics*, No. 1994-05 in Von Karman Institute Lecture Series, 1994.
15. Peraire J, Vahdati M, Morgan K, Zienkiewicz OC. Adaptive remeshing for compressible flow computations. *Journal of Computational Physics* 1987; **72**: 449–466.
16. Liu X-D. A maximum principle satisfying modification of triangle based adaptive stencils for the solution of scalar hyperbolic conservation laws. *SIAM Journal of Numerical Analysis* 1993; **30**: 701–716.

